ADVANCED ENERGY MATERIALS
www.advenergymat.de

# Operando Radiography and Multimodal Analysis of Lithium–Sulfur Pouch Cells—Electrolyte Dependent Morphology Evolution at the Cathode

*Rafael Müller,* Ingo Manke, André Hilger, Nikolay Kardjilov, Tom Boenke, Florian Reuter, Susanne Dörfler, Thomas Abendroth, Paul Härtel, Holger Althues, Stefan Kaskel, and Sebastian Risse**

**In recent years, the technology readiness level of next-generation lithium–sulfur (Li/S) batteries has shifted from coin cell to pouch cell dimensions. Promising optimizations of the electrodes, electrolytes, active materials, and additives lead to improved performance and cycling stability. However, new challenges arise with the pouch cell design and engineering (including electrode stacking and electrolyte filling), which influence the mechanistic processes of the cell. This study presents an unprecedented multimodal operando investigation of Li/S batteries on a pouch cell level and provides an inside view of material transformations during battery cycling, using X-ray radiography, electrochemical impedance spectroscopy, and spatially resolved temperature monitoring. With the comparison of two different electrolytes, new experimental details about sulfur and lithium sulfide deposition and dissolution processes are revealed and related to electrolyte and temperature distribution. Operando impedance measurements on monolayer pouch cells yield a clear correlation of electrochemical and macroscopic radiographic observations. Understanding the monolayer cells' behavior represents an optimal foundation for further studies on multilayer pouch cell prototypes and demonstrators with the developed operando setup. Herein the proof of principle for correlated measurement methods on pouch cell level is shown, and the experimental proof of concept for sulfur crystal suppression in sparingly solvating electrolyte is visualized.**

## 1. Introduction

Li/S batteries, with a theoretical energy density of 2500 Wh $kg^{-1}$, are the most promising candidates for the next generation of lightweight energy storage.[1,2] They offer higher specific theoretical capacity (1675 Ah $kg^{-1}$) and use more environmentally friendly and ubiquitous cathode materials compared to conventional lithium-ion batteries.[3] However, their widespread commercialization is hampered by the problem of capacity degradation during cycling, even in the state-of-the-art ether-based electrolyte: Lithium bis(trifluoromethanesulfonyl)imide) (LiTFSI) in 1,2-dimethoxyethane/1,3-dioxolane (DME/DOL) with $LiNO_3$ additive. These degradation processes have various origins and are caused, for example, by the so-called polysulfide shuttle effect.[4–6] The diffusion of soluble polysulfides from the cathode side to the anode lowers the coulombic efficiency and may lead to irreversible chemical reactions. This gradual consumption of active material and electrolyte and the corrosion of the metallic lithium anode lead to battery degradation. Another major challenge of Li/S batteries on their way to commercialization is the electrically insulating properties of the two end products of the cathode after charging (elemental sulfur) and discharging (lithium sulfide, $Li_2S$). To still achieve the highest possible energy density, carbon is used as the cathode host. Carbon is exceptionally lightweight and offers many different synthesis routes being able to selectively adjust material properties such as porosity, surface functionalization, wettability, and conductivity.[7–11]

Many improvements in Li/S battery performance have been achieved in recent years through materials science

R. Müller, S. Risse
Institute for Electrochemical Energy Storage (CE-AEES)
Helmholtz-Zentrum Berlin
Hahn Meitner Platz 1
14109 Berlin, Germany
E-mail: rafael.mueller@helmholtz-berlin.de;
sebastian.risse@helmholtz-berlin.de

The ORCID identification number(s) for the author(s) of this article can be found under https://doi.org/10.1002/aenm.202103432.



**DOI: 10.1002/aenm.202103432**

I. Manke, A. Hilger, N. Kardjilov
Institute for Applied Materials (CE-IAM)
Helmholtz-Zentrum Berlin
Hahn Meitner Platz 1
14109 Berlin, Germany

T. Boenke, F. Reuter, S. Dörfler, T. Abendroth, P. Härtel, H. Althues, S. Kaskel
Fraunhofer IWS
Winterbergstraße 28, 01277 Dresden, Germany

T. Boenke, F. Reuter, S. Kaskel
Technische Universität Dresden
Inorganic Chemistry I, Bergstr. 66, 01069 Dresden, Germany

approaches.[12,13] However, most publications work with the coin cell format, which provides only limited information about the practically viable pouch cell format. The scaling up of coin cells toward multilayer pouch cells offers many challenges ([14] and references therein,[15]) and benefits from observations with comparable intermediate monolayer pouch cells. This transition can be found in recent work and emphasizes the need to sharpen awareness at the monolayer cell level to avoid pitfalls during large-scale pouch cell development.[16–19]

The pouch geometry typically allows for the minimization of significant electrolyte and lithium excess, primarily for multilayer cells. In addition, electrolyte, active material, and pressure distribution become more critical for large electrode assemblies. Uniform coverage of materials and reactivity over the full electrode body is an important factor for reproducible cell manufacture. A post mortem analysis related shuttle and passivation effects to the sulfur/electrolyte ratio by visual inspection.[20] Additional theoretical work on electrolyte distribution in LiS cells done by Shi et al.[21] identifies depletion of electrolyte in the cell center. They conclude that planar electrolyte diffusion will effectively alleviate the planar heterogeneity in electrolyte distribution and electrochemical reaction.

The precise impact of deviations, like electrolyte excess and separator wrapping at the cell edges and internal concentration gradients, is still unclear and should be evaluated.

An essential prerequisite for the superiority of Li/S batteries in terms of energy density compared to other storage solutions is working under lean electrolyte conditions. However, this again leads to new limiting mechanisms that were not previously apparent. For example, releasing more significant amounts of polysulfides in ether-based electrolytes with simultaneously small electrolyte volumes can cause an enormous increase in viscosity, which drastically decreases the ionic conductivity in the battery cell.[22] This process significantly reduces the energy as well as the power density.

One approach to minimizing polysulfide shuttling is to reduce the polysulfide solubility of the electrolyte by adding selective solvents.[23–26] One of these selective solvents is the hydrofluoroether 1,1,2,2-tetrafluoroethyl-2,2,3,3-tetrafluoropropyl ether (TTE), which lowers the polysulfide solubility and the viscosity of the electrolyte as co-solvent, but does not participate in the solvation of lithium ions.[23,24,27] In previous work from our group,[24] an electrolyte containing tetramethylene sulfone (TMS) and TTE showed low polysulfide solubility. A multilayer pouch cell with this electrolyte reached a capacity of 3.7 Ah and was successfully cycled for more than 40 cycles with a comparably low electrolyte/sulfur ratio of 2.57 µL $mg_S^{-1}$. Unlike a reference cell with the state-of-the-art DME/DOL electrolyte with $LiNO_3$ as an additive, the TMS/TTE electrolyte did not show any gas formation or swelling of the pouch cell during cycling as reported by BASF and SION Power in 2017.[28] These investigations clearly show that promising sparingly polysulfide solvating electrolyte approaches for Li/S pouch cells exist even if their mode of action has not yet been fully understood. Therefore, investigating the phase changes and the resulting properties at the pouch cell level is a crucial step for the successful commercialization of this sustainable and environmentally friendly battery system.[14,29]

### 1.1. Operando Approach

Operando methods for the characterization of (dis-)charge processes in batteries have been already demonstrated to gain completely new insights into the crucial transformation, distribution, and degradation processes in various systems, i.e., Li-ion,[30] Li/S,[31–36] and Li-ion with silicon as anode.[37] However, most studies are performed with the coin cell format due to its simpler feasibility, especially in terms of material quantity and processing. Furthermore, only one characterization method is used in most cases, limiting the perspective on specific battery processes. Although a certain number of Li/S pouch cell studies[15,38,39] already exist, operando measurements with this cell type are rather the exception. Typically, applied methods cover UV–vis,[40,41] XRD,[42] XES,[43] and calorimetry.[44]

To obtain a complete and more realistic picture of the relevant processes in a Li/S battery, we have developed a setup for pouch cells that allows simultaneous measurement of temperature distribution, pouch cell stack pressure, electrochemical impedance spectroscopy (EIS), and X-ray imaging during (dis-)charging. This combination of four independent measurements during cycling provides simultaneous information on the morphology change of the electrodes (X-ray imaging), the evolution of solution or charge transfer resistances (EIS), local heat generation as well as heat dissipation, and mechanical breathing of the battery cell (force measurement). The force variations of the monolayer cells investigated herein have been below the applicable detection range, but preliminary tests with multilayer cells provided promising results. **Figure 1**A shows a 3D image of this setup, Figure 1B shows the design in the experimental setup in the µCT facility. The different morphologies of the electrodes in the initial state (left), in the discharged state (middle), and charged state on the right are shown in Figure 1C. The pressure (middle) and eight temperature sensors are well visible by their edge contrast. While the black rectangle on the left marks the zoom range used for detailed images, the white outer rectangle shows the entire pouch cell area. Here, we present an operando study on Li/S monolayer pouch cells with different sulfur loadings in a carbon nanotube-based cathode scaffold and two different electrolyte systems, the standard DOL/DME (DD) electrolyte and the sparingly solvating TMS/TTE (TT) electrolyte.[22,29] The limitation to single electrode layers allows the most lucid distinction of electrolyte and active materials distribution separately with minimal interference. Observation of inhomogeneous electrolyte distribution and edge effects herein provide the basis for analysis of multilayer cells, where such effects are present as well, albeit complexed by the overlap of several stack layers in transmission images. The resulting average attenuation of multilayer cell radiographs renders individual layer inhomogeneities more obscured while collective planar cell properties are enhanced. The magnitude of pressure and temperature changes is more pronounced in multilayer cells as well. The directly correlated results of this multimodal

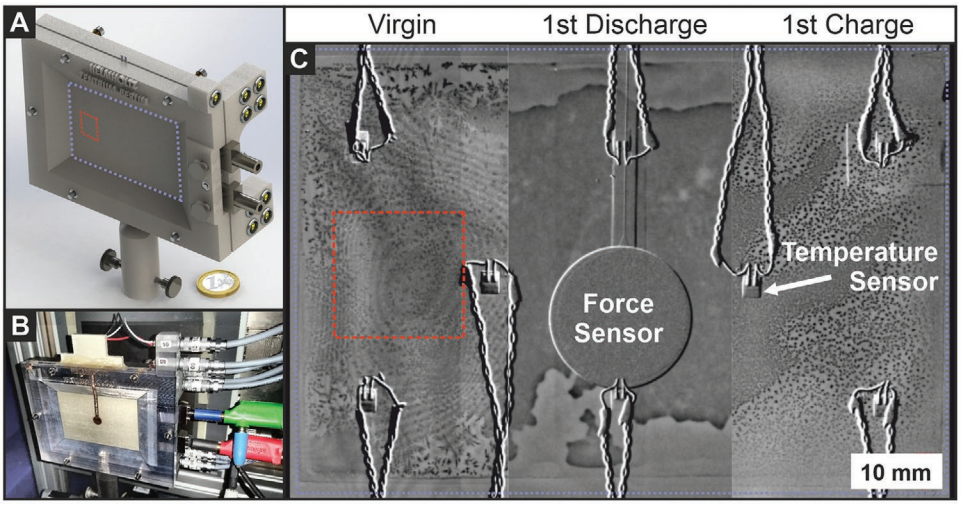


**Figure 1.** A) Setup design, B) Assembled setup, C) Three sections of radiography images: Initial state (left), discharged state (mid), and charged state (right) with marked full cell image (blue-dashed rectangle), focus view image region (red-dashed rectangle), force sensor (mid), and eight temperature sensors (white arrow) with twisted cable connections.

analysis approach clearly show its great potential for gaining knowledge about relevant cycling and degradation processes in Li/S pouch cells.

## 2. Results and Discussion

Based on previous studies, a reference system with DD electrolyte and CNT buckypaper with 30 wt% infiltrated sulfur loading (DD30) has been compared with an analogous TT30 cell and a cell with optimized sulfur loading (DD50).[29] The sulfur loading was restricted to 50 wt% as the intrinsic porosity of the employed commercial buckypaper is limited, and the cathodes with higher loading were evaluated less stable in terms of rate capability.

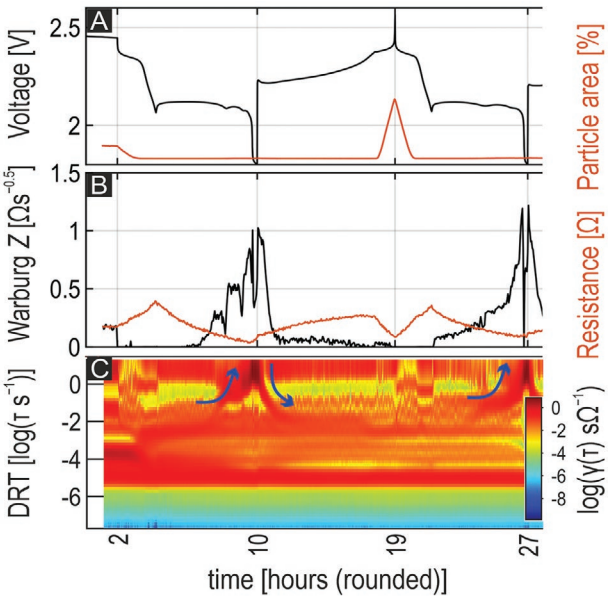


**Figure 2.** First cycle results of the monolayer pouch cell DD30 (30 wt% sulfur, DME/DOL electrolyte, charge rate 0.1 C) versus time. A) Voltage curve and sulfur particle area, B) Warburg impedance coefficient and solution resistance, C) Distribution of relaxation times. Blue arrows indicate the shift of the peak maximum in the high DRT region.

In the following, first, the results of the operando study on the DD30 cell (ether-based electrolyte, 30 wt% sulfur loading) will be presented and then compared with the results of the other two cells. The DD30 cell was cycled for nine days (a total of 38 cycles) in the operando setup. **Figure 2** introduces the results of the operando EIS analysis for the first cycle. Figure 2A: The DD30 cell was first held in OCP for 1 h, and then the hybrid EIS script was started for the remaining electrochemical measurements. In the next hour, no DC current was applied before the cell was cycled with 0.1 C for three cycles. Radiographic images were taken with the cell placed in two different magnification positions. For the three initial cycles, full cell area images were collected. Then, the cell was moved to the high magnification position, and the charge rate was set to 0.3 C. Given charge rates herein always refer to both the charging and discharging rate. During cycling, the cell exhibited the typical characteristics of a Li/S battery with an ether-based liquid electrolyte. Upon discharge, a voltage minimum is found at roughly 30% degree of discharge between the high and low voltage plateaus. This is a typical feature for ether-based electrolyte systems, indicating an increase in polysulfide species in solution, which results in a significant rise in electrolyte viscosity.[45] Additionally, the formation of undissociated medium chain length polysulfide clusters can lower the electrolyte ionic conductivity.[46] A direct consequence of this process is the presence of a local maximum in the solution resistance ($R_S$), which is derived from the high-frequency region of the operando EIS measurements and is shown in Error! Reference source not found.[47–51] A combination of pore coverage simulation and EIS modeling shows a similar maximum of resistance at a corresponding degree of discharge.[52]After the concentration of polysulfides drops again by electrochemical reduction and lithium sulfide formation, the solution resistance decreases, and the Warburg impedance increases due to the depletion of polysulfides

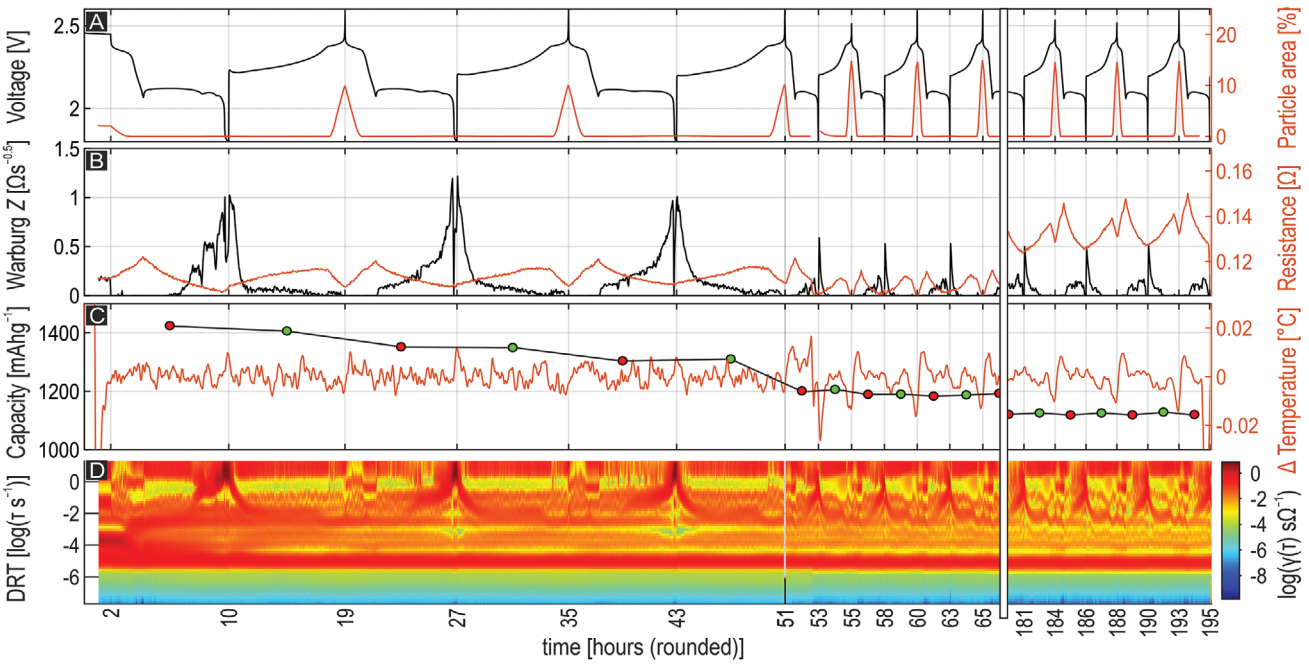


**Figure 3.** Cycling overview of the monolayer pouch cell DD30 (30 wt% sulfur, DME/DOL electrolyte) versus time. A) Voltage and sulfur particle area, B) Warburg impedance coefficient and solution resistance, C) Capacity and temperature, D) Distribution of relaxation times. The first three cycles at charge rate 0.1 C are shown, and the first and last four cycles at 0.3 C in the radiography zoom position. The *x*-axis is cut to fit all data.

at the cathode surface. The rise in Warburg impedance during discharge is accompanied by a gradual increase in the charge transfer resistance for slow processes. This effect can be traced in the upper range ($\tau = 10^{-2}$ to 1 s) of the distribution of relaxation times (Figure 2C). **Figure 3** shows an extended overview of the cell performance during X-ray image acquisition. The Warburg impedance reaches its maximum in the discharged state and drops more rapidly in the subsequent charge step than during its rise. This discrepancy indicates that the dissolution process of the surface blocking[53] lithium sulfide particles is faster than their formation process. While the cell is charged, another local maximum of the solution resistance is formed where the voltage curve describes a step. Again, as during the discharge, this is attributed to an increase of the polysulfide concentration accompanied by a rising viscosity of the electrolyte.

Similar polysulfide distribution effects have also been shown by operando X-ray fluorescence studies on ether-based Li/S cells,[33] and their impacts are discussed in more detail later in the chapter comparing different electrolytes. Following the step in the voltage profile during charging, the drop of solution resistance can be explained by the transformation of dissolved polysulfides to solid sulfur phases, which can clearly be seen in the radiographs of charged cells (**Figure 4**E, and DD30 Videos SV1 and SV2 in the Supporting information). The semi-quantitatively determined particle area is plotted in the upper left inset of Figure 4.

### 2.1. Imaging Results

Operando radiography provides insights into the pouch cells during operation, and the images of the first cycle of cell DD30 are correlated to its voltage curve in Figure 4. The respective radiographic results at marked cell states are illustrated, and a full video of the operando radiography during cycling can be found in Video SV1 (Supporting Information).

Marker A is assigned to the initial state of the cell before the application of a discharging current. Figure 4A shows a distribution pattern of the melt impregnated sulfur loading. XRD measurements of pristine cathodes have confirmed the presence of sulfur in its stable $\alpha$-modification.[54,55] The small features with sharp contrast are thus attributed to solid $\alpha$-sulfur crystallites. Over more extensive regions of the cell domains with smooth contrast, differences are visible, which indicate concentration gradients of dissolved sulfur species or dynamic electrolyte absorption (variation in thickness or composition concerning the median image). Figure 4B depicts the intermediate state of the first discharge. All solid sulfur is dissolved, and the cell area appears almost featureless. Only the sensors and cables outlines appear edge-enhanced due to the strong absorption of their materials and a slight rotation of the cell. This effect cannot be removed by linear translation registration of the images. Nevertheless, this image shows how well static features inside of the cell, like the electrode edges and tabs, are lessened.

A very slight outline of the shape that evolves toward the discharged state in Figure 4C can be recognized. A contrast front of presumably enriched lithium sulfide deposition is formed in the discharged cell state. The front bears some similarity to the gradual contrast domains seen in the frame (A), but individual lithium sulfide nanoparticles are not resolved.[11] It is known from previous studies that $Li_2S$ crystals are usually occurring in the nm range during cycling. Further aspects of $Li_2S$ formation mechanisms are discussed in Section 2.2.

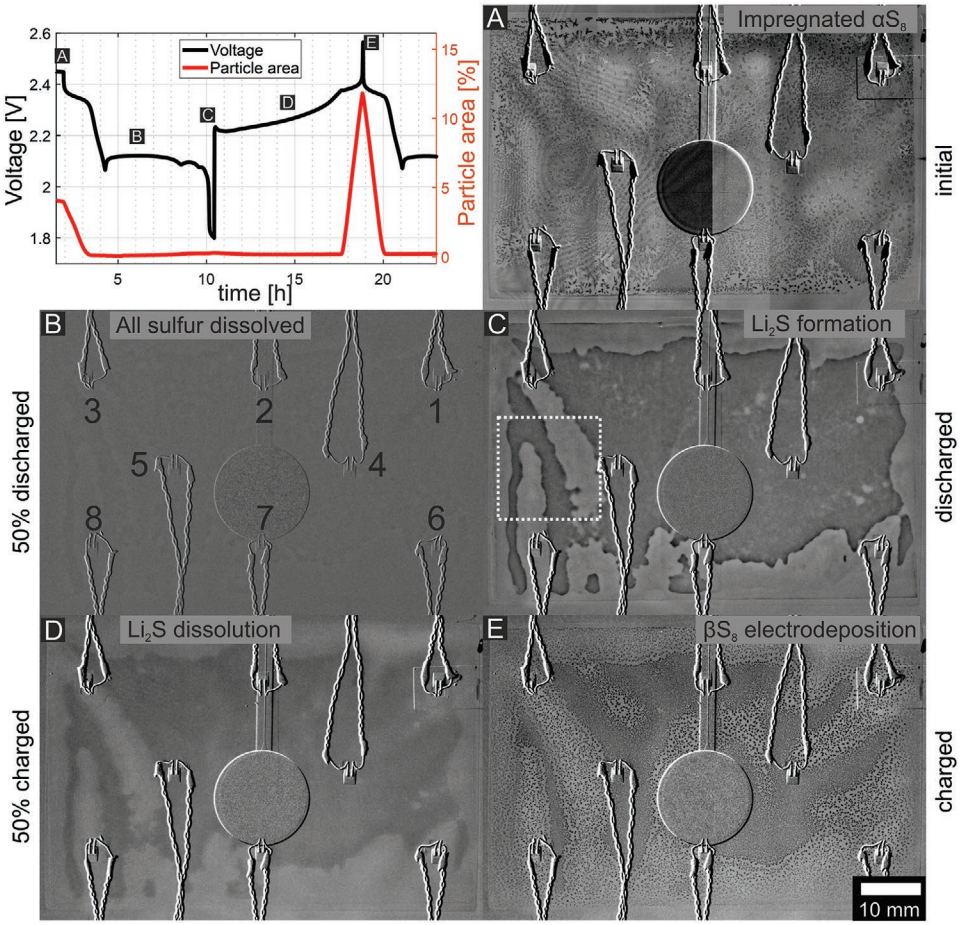


**Figure 4.** Inset: Cell voltage and particle area percentage versus time for the first cycle at 0.1 C. The particle area was determined by background correction using a rolling-ball algorithm and threshold selection. Frame (A–E): Radiographs of the cell during the first cycle. A) initial state, B) 50% discharged, C) 100% discharged, D) 50% charged, E) 100% charged. Dark patterns are attributed to dense $S_8$ and $Li_2S$ species. Sulfur exhibits the highest X-ray absorption coefficient of all the electrode and electrolyte materials. The initial frame (A) shows concentric blur and vertical shading artifacts on the left side due to a non-steady setup state during beam warm up. The numbering in frame (B) indicates the temperature sensor positions and a white rectangle in frame (C) illustrates the magnified zoom-in region.

The contrast front follows roughly a smoothed rectangular geometry of the cell with reduced size except for the more irregular left side. During the following charge, the contrast domains fade (Figure 4D) until they almost completely disappear before the beginning of visible sulfur crystallization (between Figure 4D,E, see Video SV1, Supporting Information). In the charged state, Figure 4E, the distribution of grown sulfur crystals is apparent. Clearly, a general resemblance of the crystallite size domains matches the outline of the discharged state's darker shape (Figure 4C). Direct comparison of discharged to charged state frames indicates smaller sulfur particles are formed within the darker area while enlarged particles are found at the dark contrast front. In the subsequent discharge, the small particles dissolve faster than the large ones, which is expected for typical dissolution kinetics due to simple surface-to-volume ratio considerations.

For the DD electrolyte, cells with higher unobstructed electrolyte volume show larger sulfur crystals, but the cell performance and voltage curves can apparently be very similar. This indicates that the performance characteristics are not strongly dependent on the sulfur crystal size. Sulfur crystallization and dissolution seem to be rapid enough to cause no limitation to the kinetics (at the investigated C-rates) and do not appear to be surface or transport blocking.

The similarity of individual charge/discharge cycles allows merging them by creating a mean of all cycles with the charge rate of 0.3C normalized to the state of charge. This data evaluation lessens the noise of the mean temperature data and impedance parameters profiles. **Figure 5** depicts the results of data normalization to the state of charge (SoC) and mean generation. The formation of solid sulfur particles clearly coincides with the voltage plateaus around the charged cell state between the green markings. The amount of solid sulfur, estimated by its areal fraction in radiographic images, is inversely related to the solution resistance. This observation can be explained by the lowering of viscosity and rise of diffusion rates of the electrolyte during depletion of dissolved polysulfide concentration.

At the beginning of the second plateau, the maximum solution resistance occurs at the dip in the voltage curve during discharge. It is noteworthy that this overpotential rises with increasing charge rate and may then drop under the lower voltage limit. If the discharge control implements a

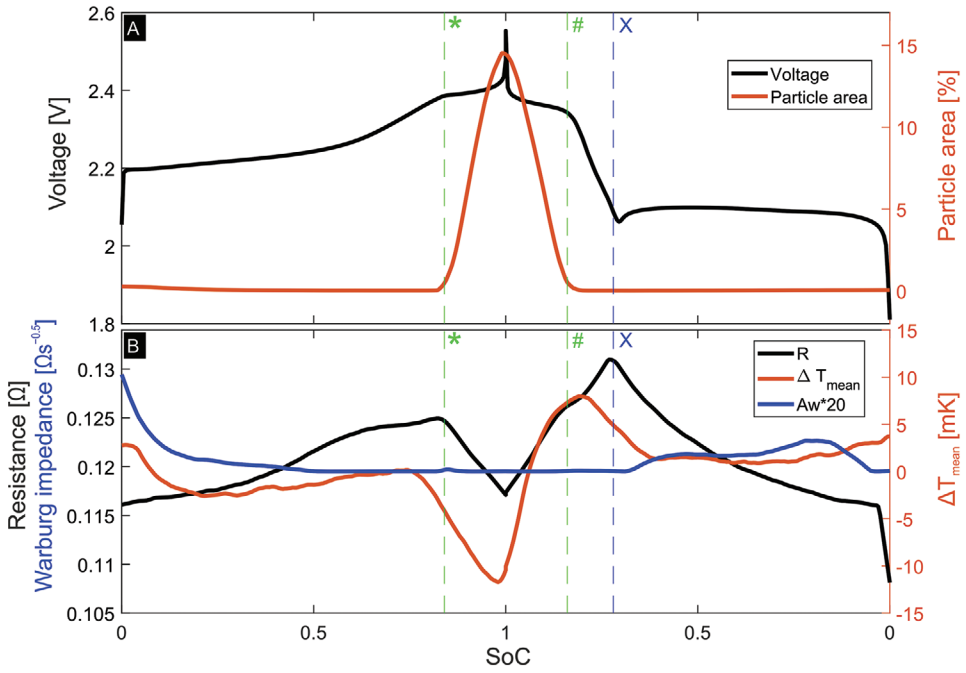


**Figure 5.** Comparison of SoC normalized voltage curves A) (black) with particle formation (A, orange), mean temperature difference B) (orange), impedance parameters solution resistance (B, black), and Warburg coefficient (B, blue). The beginning of the second charge plateau (*) and the end of the first discharge plateau (#) are marked as green vertical lines. The beginning of the second discharge plateau is marked as blue vertical line (X).

voltage-based stopping condition, the second discharge plateau is not reached at high charge rates.

The temperature appears to follow the solution resistance mainly near the charged cell state. This relative decrease of temperature was observed even for monolayer cells and contradicts the commonly observed intuitive rise of battery temperature during charging. The most heat is released during the beginning of the discharge with the maximum laying between the discharge voltage plateaus. During the second discharge plateau, a dependency on the Warburg coefficient seems to be present, especially for the TT30 cell. A detailed discussion of the temperature changes with SoC can be found in Figures S7 and S8 (Supporting Information). The highest relative temperature change rate was found in the center of the pouch cell (**Figure 6**).

Both impedance parameters, solution resistance and Warburg coefficient, must be treated with care at the end of the discharge. A severe drifting of the cell state is observed in this region, accompanied by a steep voltage drop. Our operando script is set to interrupt running EIS measurements to prevent overcharging or a deep discharge, leading to fractional EIS data that is not included in the analysis process. As a result, the data density near the discharged state is low. We consider the drop of solution resistance and the inconsistency of the Warburg coefficient compared to the start of charging as artifacts.

## 2.2. Morphology Change

Only one layer of each electrode was used in this study to investigate the morphology changes of the two electrodes. Multilayer

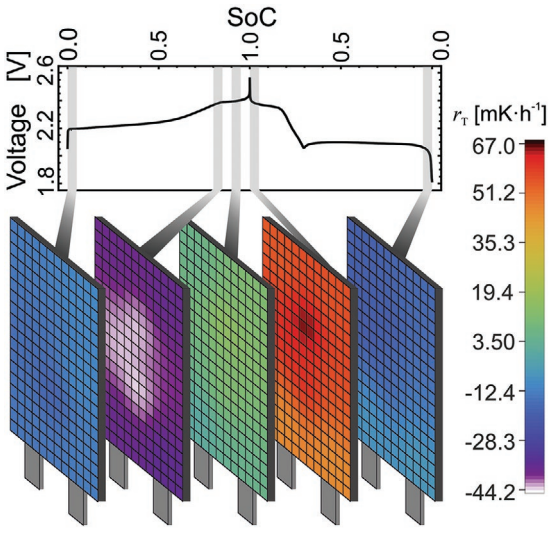


**Figure 6.** Distribution of temperature rates ($r_T$) at different states of charge of the pouch cell. The average temperature values of ten consecutive cycles were taken to minimize data noise. The spatially resolved temperature rates were determined using the eight Pt100 sensors. The gray areas in the voltage curve mark the averaging intervals for the individual rates. While the temperature hardly changes for small values of SOC, there is a significant cooling in the center of the pouch cell in the initial region of the second charge plateau (80–85% SOC). In the subsequent discharge step (100–95% SOC), the center of the pouch cell is clearly heated. The hottest spot is at a position shifted away from the pouch cell tabs because they introduce a higher heat exchange with the environment, and therefore equilibration rate.

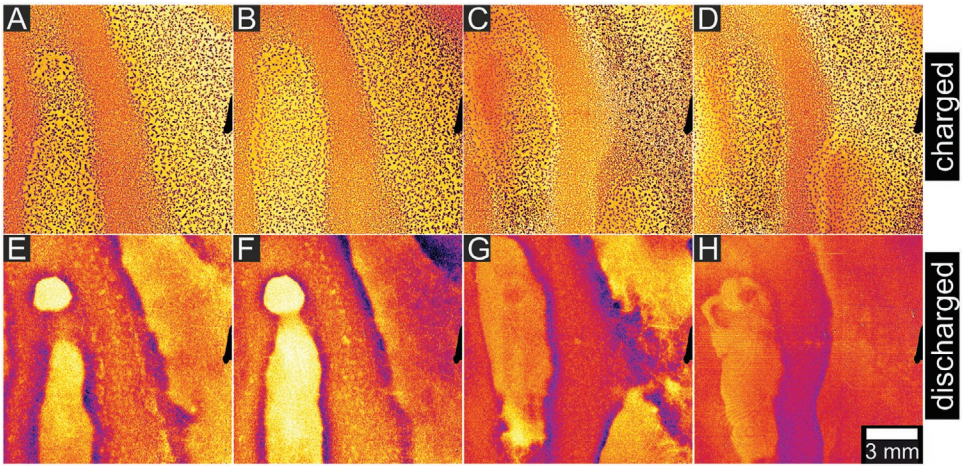


**Figure 7.** Contrast-enhanced radiography images of the 30% DOL/DME cell during cycling at 0.3 C. A–D) Charged cell states of cycles 1, 6, 21, 31 at 0, 27, 96, 141 h; E–H) Discharged cell states of cycles 2, 6, 22, 32 at 8, 24, 98, 143 h. (No images were acquired during a weekend beam shutdown).

pouch cell investigations are planned in further follow-up studies, and the applicability of the setup has already been confirmed experimentally for this case. However, wrinkles in the pouch foil, which can lead to an inhomogeneous electrolyte distribution, can hardly be prevented when manufacturing monolayer pouch cells, and edge effects (like excess electrolyte reservoirs) can be observed in all pouch cells. At the same time, this opens up the opportunity to consider this configuration as a model system to investigate the influence of such inhomogeneous starting conditions on the morphology evolution of the electrodes. This influence can be seen very well on the enlarged X-ray images in **Figure 7** (see also Video SV2 in Supporting Information). The magnification range is marked by the small white rectangle in Figure 3C. A collection of all magnified images of the charged and discharged cell states of DD30 is provided in Figures S11 and S12 (Supporting Information).

While particularly large sulfur crystals form in the charged state in the area of the folds, mainly smaller crystals can be seen in the areas with smaller electrolyte excess (Figure 7A). This pattern continues over many cycles (Figure 7B,C), with the area with the larger sulfur crystals appearing to expand with cycle number. These crystallization dynamics are in good agreement with nucleation and growth theory.[56] The determining factor for the different crystal sizes is the nucleation density in the cathode, which depends directly on the time variation of the polysulfide concentration. The polysulfide concentration changes more slowly in areas with more electrolyte volume than in areas with less electrolyte due to equilibration of the concentration gradient with the electrolyte reservoir. This process is mediated by the dis- and comproportionation reactions of $Li_2S_x$ species. With electrolyte excess, fewer nuclei are available for the subsequent growth of the sulfur crystals, extending hundreds of micrometers in size into electrolyte volumes, if available. This condition leads to a distribution of particularly large sulfur crystals in the areas with low nucleation concentrations.

Another aspect that tends to increase this effect is that in the areas with more electrolyte volume, the metallic lithium anode is more exposed to the polysulfides that are known to have a passivating effect[57] at such locations. Consequently, the lithium-ion exchange is hindered and thus further reduces the temporal polysulfide gradient during charging.

Due to the spatial resolution of the X-ray setup of 5–8 µm at most, visualization of individual nanoscopic lithium sulfide crystals is not possible.[11] However, distinct inhomogeneous depositions can be seen in the X-ray images in Figure 7E–H. Since short-chain polysulfides and lithium sulfide are more difficult to dissolve and tend to form clusters,[46] the critical deposition concentration is already reached very quickly at the (pore)surface site of electrochemical reduction. It can be assumed that the longer path of the lithium ions in the thicker cell area with a lot of electrolyte volume and higher distance between the electrodes lead to an inhomogeneous current density of the lithium ions on the cathode.

Considering both increased relative current density and higher concentration gradient in thin electrolyte domains, a faster nucleation and growth rate for $Li_2S$ deposition occurs in these areas. While the inner parts of the flat cell domains deplete the dissolved polysulfides during discharge, the edges of the thin domains have access to the larger polysulfide reservoir of the excess electrolyte domains where the $Li_2S$ nucleation is slower, leading to accumulated $Li_2S$ deposition at the boundaries. These contrast fronts are found initially at an outer rim resembling roughly the rectangular pouch cell shape and at wrinkles. On the X-ray images in Figure 7E–H, these outlines with higher X-ray absorption at the wrinkled area are well observable. The temporal change of these outlines in the discharged state also clearly reflects the areas of the different sulfur crystals from the charged state. Due to the concentration of $Li_2S$ in the contrast front regions, a particularly large number of polysulfides are released here in the subsequent charging steps. Dynamic gradual redistribution of preferred $Li_2S$ deposition area spreads out like a front from cycle to cycle. This process can be seen on the X-ray images by the gradual increase of the areas with low X-ray transmission. A mechanic deformation of the packing foil and its wrinkles due to the electrode volume changes cannot be excluded and may influence the shifting of these areas. The contrast fronts appear not to

be locally persistent for prolonged cycling, which makes permanent passivation unlikely to explain the observed lateral differences. The development of prevalent $Li_2S$ seeds[58] leading to preferential $Li_2S$ growth might occur, but the moving front indicates a reversible nucleation mechanism[53] over extended cycling. The dimensions of $Li_2S$ deposition cannot be resolved, but a high specific surface[59] and redox mediators are proposed possibilities to mitigate surface blocking by 2D $Li_2S$ coverage.[60] A sophisticated computational 3D-model has been developed to describe the porous microstructure of Li/S batteries.[61] The modeled system largely agrees well with our findings, although the radiographically shown occurrence of sulfur micro crystals indicates their growth is not confined to pores or surfaces.

For multilayer pouch cells, a more uniform initial electrode stack is expected, but long-term investigations are required to determine whether small initial differences can lead to concentration or equilibration of inhomogeneities.

### 2.3. Electrolyte Comparison

For the TMS/TTE electrolyte, significantly different behavior of the sulfur phase transformations is observed. In the charged state, no solid particles above the dissolution limit (≈5 µm) can be detected, neither for $Li_2S$ nor for sulfur (**Figure 8**C). The cell voltage curves show oxidation of sulfur to its elemental state during the charging process. Considering the low solubility of elemental sulfur in the TMS/TTE electrolyte, a solid sulfur phase is expected. It can be concluded that sulfur is deposited in a small microcrystalline form or precipitates as nanoparticles.

Furthermore, these results also confirm the assumptions made for the ether-based electrolyte in the DD30 and DD50 cells. According to nucleation and growth theory and due to the limited concentration of polysulfides in the TT30 cell (see Video SV3 in Supporting Information), very rapid changes in sulfur concentration can be generated during electrochemical oxidation, resulting in very large numbers of nuclei for sulfur crystallization. Following this assumption, the dense distribution of smaller sulfur particles can, therefore, no longer be imaged with the resolution of the X-ray system used.

The electrochemical voltage curves (**Figure 9**) have been normalized regarding their state of charge. The resulting curves (Figure S1, Supporting Information) show a relatively steady general shape, indicating stable cell behavior. DD30 shows a few minor waves in the second discharge plateau during the first discharge cycle. This observation can be attributed to the equilibration of electrode wetting, conditioning and solid electrolyte interphase conditioning.[62–65]

An increased overpotential of the second discharge plateau in all cells is observed for the 0.3 charge rate compared to 0.1 C. This effect is stronger for the DD50 cell than for the 30% sulfur-loaded electrodes in DD30, and it is slightly stronger in TT than in the DD electrolyte. The rise is attributed to the higher current density per electrode area and the higher concentration of long-chain polysulfides. While the SoC normalized voltage curves of the cells with 30% sulfur loading show good overlap for increasing cycle numbers, the voltage dip after the first discharge plateau of DD50 at 2.0 V moves toward lower SoC (35–23%) during cycling. This means a lesser relative charge is required to reach the maximum polysulfide concentration. In this study, the TT30 cell showed a relatively long first discharge plateau compared to other coin and pouch cell experiments that are not included herein. This shift appears to be related to the excess electrolyte used for the monolayer pouch cells. Further data is required to strengthen this hypothesis, which will be part of the future evaluation.

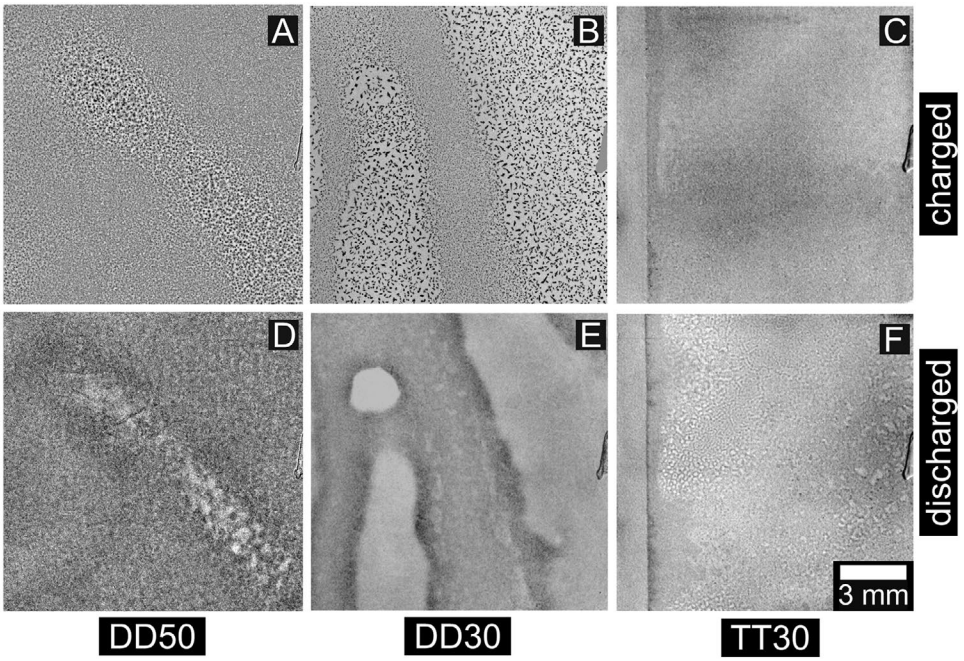


**Figure 8.** Radiographic image comparison of three pouch cells with different electrolytes and sulfur loading: Top row images are in charged state, bottom row images are in discharged states. Electrolytes, loadings: A,D) DOL/DME, 50% S; B,E) DOL/DME, 30% S; C,F) TMS/TTE, 30% S—The same overview of full cell images is shown in Figure S10 (Supporting Information).

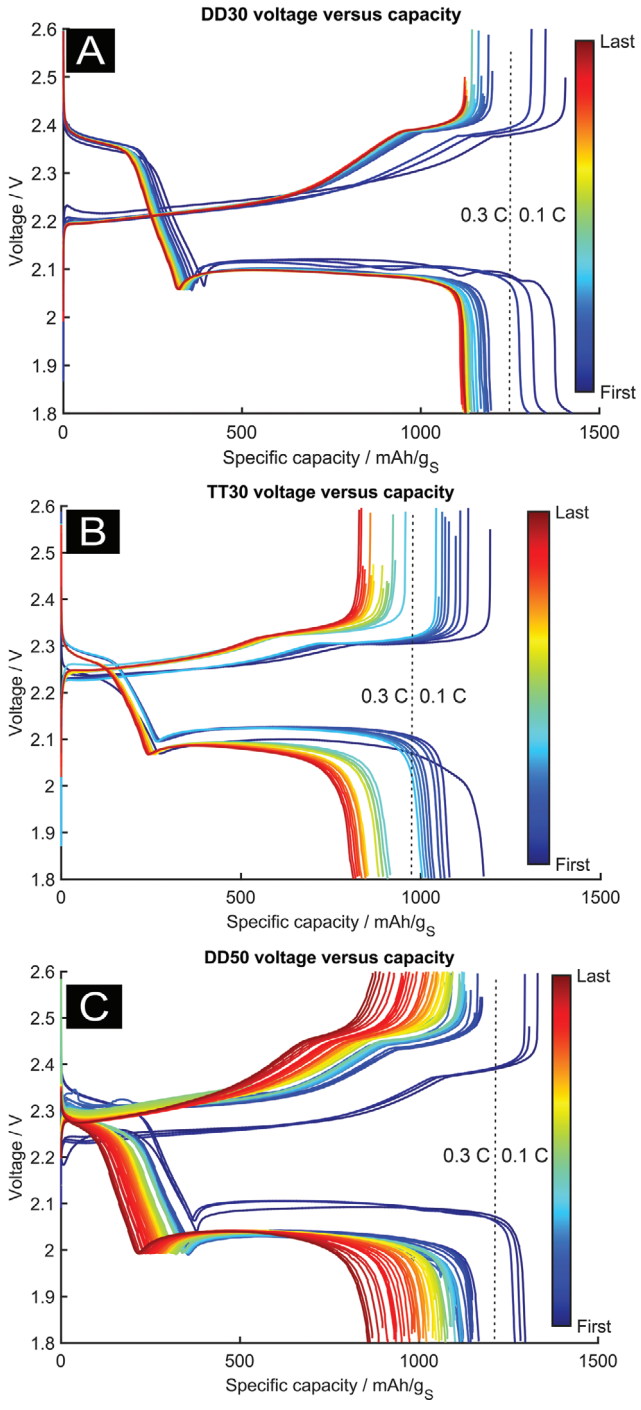


**Figure 9.** Voltage curves during cycling of A) DD30, B) TT30, C) DD50. For the first cycles a charge rate of 0.1 C was used and for the following cycles 0.3 C was applied as charge and discharge rate. The dotted line marks the switch of the charge rate. DD50 cycling was interrupted after the 6th cycle for a weekend in resting state.

The EIS data comparison of the three cells shows qualitatively similar shapes (Figure S2, Supporting Information), albeit with varying degrees of noise due to ongoing parameter optimization (i.e., magnitude of alternating current and limiting conditions). The temporal evolution of EIS parameters versus time can be found in Figures S3–S5 (Supporting Information) together with a plot of performance descriptors (Figure S6, Supporting Information). The solution resistance maxima are located at the voltage ramps between the voltage plateaus. The DD50 cell shows the most pronounced difference of minima and maxima during cycling (0.1–0.5 Ohm). For the TT30 cell, a high starting solution resistance of 0.4 Ohm is observed, as expected from the sparingly solvating electrolyte properties and higher electrolyte viscosity (Figure S13, Supporting Information). The height of the local maxima is comparably small with 0.1 Ohm. This small change of solution resistance is expected from the ex situ results due to the limited polysulfide solubility in the TT electrolyte.

The DD30 cells' solution resistance initially started at around 0.1 Ohm, but it shifted to 0.14 Ohm with cycling. The respective maxima are only up to 0.02 Ohm higher than the minima. This low solution resistance change likely derives from the low dynamic polysulfide concentration equilibrium, expected for electrolyte excess systems. In the discharged state, Warburg impedance maxima are found for all cells. Proper fitting is limited in severe cell voltage drift regions, especially at the higher charge rate of 0.3 C, leading to artifacts visible by interrupted curves. The Warburg coefficients' order of magnitude can be well estimated for the charge rate of 0.1 C, though. The TT30 cell's value is rough twice the value of the DD cells, and the impact of the electrolyte viscosity difference seems to contribute most to this diffusion limitation descriptor.

## 3. Conclusion

The developed multimodal setup with the operando analysis methodology has successfully been applied to Li/S monolayer pouch cells, and morphologic discrepancies regarding different locations could be elaborated. The proof-of-principle has been established and provided clear experimental evidence that no macroscopic sulfur crystallites occur in the sparingly polysulfide-solvating TMS/TTE electrolyte, in contrast to ether-based DME/DOL electrolyte with high polysulfide solubility. In the ether-based DOL/DME electrolyte, the sulfur loading and the local excess electrolyte distribution play critical roles in the sulfur crystallization and dissolution kinetics.

The DD50 cell with higher loading showed more homogeneous sulfur and $Li_2S$ distribution than the low loading DD30 cell. This may be an effect of an increased overall polysulfide saturation leading to lower local distribution gradients, or facile more flat assembly. A radial electrolyte volume distribution effect has been detected during cell cycling. This appears as a concentric reaction front expansion during charge and discharge. A reverse contracting motion occurs after switching the current. Additionally, a general trend of sulfur crystallization from the cell center toward the pouch cells' edges and wrinkle areas was observed, and these local formation dynamics were similar for DD50 and DD30. The combined observations can most likely be explained by excess electrolyte volume distributions.

Nevertheless, a contribution from conversion rate shifts from the cell center due to temperature or conductivity gradients or volume change driven mass migration of a combination

of several effects cannot be excluded at this stage. The cell with sparingly polysulfide solvating electrolyte TT30 showed the periodic shifting of broad unsharp contrast domains, resembling gradual electrolyte volume change rather than unresolved solid particle distribution. The microscale crystallization behavior appears to be less affected by electrolyte distribution variation in this system compared to the DD cells. The initial voltage of the TMS/TTE cell is lower than the DD cells, but a similar voltage is reached after the first discharge plateau.

Electrolyte characteristics have been compared, and diffusion-related impedance results are consistent with viscosity measurements. This match validates the aspect of the design strategy that applies polysulfide solubility limitation to mitigate the shuttle effect. Operando temperature distribution analysis revealed that a temperature change of the pouch cell is strongly related to the inner resistance and sulfur crystallization process, and the temperature distribution is governed by the cell geometry and tabs placement. The main factors under the investigated conditions are probably joule heating and the heat transfer rate to the environment. Overall, a sound foundation for detailed industrially relevant pouch cell operando analysis has been developed from setup via validation to application on prototype cells. The obtained insight confirms electrolyte development strategies and reveals potential for mechanistic process determination and kinetic behavior monitoring.

## 4. Experimental Section

*Pouch Cell Assembly*: Commercial freestanding carbon nanotube electrodes (MWNT Blend Buckypaper, NTL) were used without further treatments and cut to the final pouch cell size (71 × 46 $mm^2$). Sulfur powder (Alfa Aesar, >99.5%) was mixed with a non-toxic volatile surfactant in a ball mill for 10 min to form a viscous sulfur suspension (30 wt% Sulfur). This slurry was tape-casted onto custom-made aluminum transfer foils (20 µm, MTI). The specific sulfur loading was controlled by doctor-blading an appropriate wet film thickness. The sulfur sheets were dried for 10 min at 80 °C and kept at room temperature overnight. The carbon-based electrodes were placed on the sulfur foils in a steel housing container in the next step. Sulfur transfer melt infiltration was performed at 155 °C for 1 h in an argon atmosphere. Subsequently, the buckypaper/sulfur electrode was laminated onto a carbon-primered aluminum foil (20 µm, MTI). The monolayer pouch cells were assembled in a glove box with argon atmosphere (MBraun, <0.01 ppm $O_2$ and $H_2O$). Lithium metal foil (thickness: 50 µm, CEL China Energy Lithium Co., Ltd) and PE separator foil (thickness: 12 µm) were used for the cell assembly. Further details of the cell manufacturing steps and electrode materials characterization can be found elsewhere.[29]

The prepared pouch cells were filled with 1 mL electrolyte each. The chemicals for both electrolytes were purchased from Sigma Aldrich without further purification. The ether-based electrolyte (DD) consists of a mixture of 1,3-dioxolane and 1,2-dimethoxyethane (DOL/DME, v/v 1:1), 1.0 M lithium bis(trifluoromethanesulfonyl)imide (LiTFSI), and 0.5 M $LiNO_3$. The sparingly solvating electrolyte (TT) consists of sulfolane and 1,1,2,2-tetrafluoro-3-(1,1,2,2-tetrafluoroethoxy)propane (TMS/TTE, v/v 1:1), and 1.5 M LiTFSI. In this operando study, three different cells were investigated. The respective cell parameters and their short designations are summarized in **Table 1**.

*Operando Setup*: This study's operando pouch cell setup was developed to allow simultaneous measurement of different cycle parameters. The cell holder was designed using CAD software and then printed using a 3D printer and a UV-curable resin-based plastic (VeroBlack). This plastic offers very high stability and mechanical robustness. Figure 1 shows the rendered graphic of the cell holder (A), the assembled cell holder with connected sensors in the X-ray imaging measurement system (B), and the arrangement of the sensors (C). The eight temperature sensors at the back of the setup Figure 1C measure the temperature on the pouch cell surface.

They were arranged in a 2 × 3 square cell-matrix containing a Pt100 temperature sensor in its center. In addition to these six sensors, two sensors were placed on the horizontal centerline of the setup, where four adjacent squares shared corners to realize the highest possible coverage.

The temperature mapping was done by calculating the averaged nearest neighbor temperature contribution of the temperature sensors over a 12 × 18 grid pattern. On the front side of the operando setup (Figure 1C), a capacitive force sensor (singleTact.com) with 5 V operating voltage was mounted on which a maximum force of 45 N can be applied. The force measurement of this calibrated sensor was done by monitoring the DC voltage response. The linear range of the voltage signal (0.5–1.5 V) corresponds to a force of 0–45 N. To ensure that the force is distributed as evenly as possible over the entire pouch cell, a 1 mm thick polypropylene plate with the dimensions of the active area of the cell was placed between the sensor and the pouch cell.

*Electrochemistry*: Cycling of the cell was performed using an Interface 1000 potentiostat (GAMRY Instruments). A hybrid measurement script based on a galvanostatic approach was used to measure the operando EIS. It superimposes an oscillating current signal on the constant DC charging current, and the frequency-dependent AC voltage response is measured. If the measured voltage amplitude exceeds a set value, the amplitude of the oscillating current signal is reduced. Thus, this script allows continuous charging and discharging of the battery with control of the oscillation current and voltage signal amplitudes. The alternating current amplitude was set relative to the sulfur loading (1672 mAh $g^{-1}$) with C/50 (root mean square), and the maximum voltage amplitude was set to 20 mV (root mean square). The EIS script checks for the defined end-of-charge (2.6 V) and end-of-discharge (1.8 V) voltages after each measured frequency, ensuring minimal overcharge. When the end-voltage is reached, the sign of the DC current reverts, and the next cycle step starts. A tradeoff between data point density and the slow measuring, drift susceptible low frequencies is required. Thus, a frequency range from 250 kHz to 0.25 Hz with ten points per decade was used. The time-dependent DC voltage and current were extracted from each frequency point. Only

**Table 1.** Summary of relevant cell parameters of all three pouch cells used in this study.

| Name | Sulfur loading [mg] | Sulfur loading [wt%] | Areal loading[a)] [mg $cm^{-2}$] | Areal capacity[a)] [mAh $cm^{-2}$] | Electrolyte | E/S ratio [µL $mg_S^{-1}$] |
|---|---|---|---|---|---|---|
| DD50 | 63.58 | 50.56 | 1.95 | 3.25 | 1.0 mol LiTFSI + 0.5 mol $LiNO_3$ + 1 L DOL/DME (50%/50%) | 15.7 |
| DD30 | 30.79 | 33.27 | 0.95 | 1.58 | 1.0 mol LiTFSI + 0.5 mol $LiNO_3$ + 1 L DOL/DME (50%/50%) | 32.5 |
| TT30 | 27.93 | 31.32 | 0.86 | 1.43 | 1.5 mol LiTFSI + 1 L TMS/TTE (50%/50%) | 35.8 |

[a)]The electrode area was 33 $mm^2$ for all cells.

complete EIS frequency ranges were considered for the evaluation of the impedance spectra.

Before the EIS data could be analyzed with an equivalent circuit model (ECM), the data were corrected for time drift using linear interpolation between measurements. This procedure was published elsewhere[47] and is possible due to the high measurement point density, which was achieved by about 180 impedance spectra per cycle step at a charge rate of C/10. The ECM consists of four elements connected in series. In addition to a resistor for the solution resistance ($R_S$), a Warburg element ($A_W$, infinite diffusion) and a coil for the inductance of the cables (L), a distribution of relaxation times ($\gamma(\tau)$, DRT) was used to simulate the complex charge transfer processes. The fitting of the data was done by a linear algebra approach. While the Warburg Impedance is mainly dominated by the concentration of dissolved polysulfides, the solution resistance largely depends on the concentration and mobility of lithium ions.[66]

*Imaging*: The X-ray radiography measurements were performed with a µCT setup using a tungsten target and no filter.[67] The voltage and current of the X-ray tube were set to 60 kV and 166 µA, respectively. Images were taken with an exposure time of 0.8 s on a flat panel detector (Hamamatsu, C7942SK-05, 2316 × 2316 active pixels) with a pixel size of 50 µm. The geometry of the instrument with the cell setup allowed a maximum magnification of 8.6, resulting in an effective pixel size of 5.8 µm. *Post*processing of the images was done using the freely available open-source software Fiji.[68] All images were normalized with respect to a median pseudo flatfield image after dark and flat field correction. An example pseudo flatfield image and an overlay to illustrate cell domain correlations are shown in Figure S9 (Supporting Information). A temporal range between the charged and uncharged states with few morphology features was used to generate the image for this purpose. This procedure allowed the detection of small changes in the electrode structure and material distribution by removal of static cell components. Subsequently, a moving averaging of typically 10 normalized images was performed to improve the signal-to-noise ratio.

## Supporting Information

Supporting Information is available from the Wiley Online Library or from the author.

## Acknowledgements

This work was developed in the project HiPoLiS (reference number: 03XPO178) and was partly funded by the German Ministry of Education and Research (BMBF) within the research program Batterie 2020. The authors thank the project partners Wingcopter and the Fraunhofer Institute IWS, in particular, Kelly Henze for cathode preparation and Peter Fleischer for the manufacturing of the pouch cells. Special thanks to the tomography group at HZB for providing extended beamtime on the µCT imaging system.

Open access funding enabled and organized by Projekt DEAL.

## Conflict of Interest

The authors declare no conflict of interest.

## Data Availability Statement

The data that support the findings of this study are available from the corresponding author upon reasonable request.

## Keywords

lithium sulfur batteries, multimodal operando analyses, X-ray imaging, impedance spectroscopy, pouch cells, sparingly solvating electrolytes

Received: November 3, 2021
Revised: January 14, 2022
Published online: February 18, 2022

[1] S. Dörfler, S. Walus, J. Locke, A. Fotouhi, D. J. Auger, N. Shateri, T. Abendroth, P. Härtel, H. Althues, S. Kaskel, *Energy Technol.* **2020**, *9*, 2000694.
[2] M. Zhao, B.-Q. Li, X.-Q. Zhang, J.-Q. Huang, Q. Zhang, *ACS Cent. Sci.* **2020**, *6*, 1095.
[3] A. Varzi, K. Thanner, R. Scipioni, D. Di Lecce, J. Hassoun, S. Dörfler, H. Altheus, S. Kaskel, C. Prehal, S. A. Freunberger, *J. Power Sources* **2020**, *480*, 228803.
[4] W. Ren, W. Ma, S. Zhang, B. Tang, *Energy Storage Mater.* **2019**, *23*, 707.
[5] A. F. Hofmann, D. N. Fronczek, W. G. Bessler, *J. Power Sources* **2014**, *259*, 300.
[6] M. R. Busche, P. Adelhelm, H. Sommer, H. Schneider, K. Leitner, J. Janek, *J. Power Sources* **2014**, *259*, 289.
[7] C. Kensy, F. Schwotzer, S. Dörfler, H. Althues, S. Kaskel, *Batteries Supercaps* **2021**, *4*, 823.
[8] C. Kensy, D. Leistenschneider, S. Wang, H. Tanaka, S. Dörfler, K. Kaneko, S. Kaskel, *Batteries Supercaps* **2021**, *4*, 612.
[9] C. Kensy, P. Härtel, J. Maschita, S. Dörfler, B. Schumm, T. Abendroth, H. Althues, B. V. Lotsch, S. Kaskel, *Carbon* **2020**, *161*, 190.
[10] R. Fang, K. Chen, L. Yin, Z. Sun, F. Li, H. M. Cheng, *Adv. Mater.* **2019**, *31*, 1800863.
[11] S. Dörfler, P. Strubel, T. Jaumann, E. Troschke, F. Hippauf, C. Kensy, A. Schökel, H. Althues, L. Giebeler, S. Oswald, S. Kaskel, *Nano Energy* **2018**, *54*, 116.
[12] S. Lang, X. Feng, J. Seok, Y. Yang, M. R. Krumov, A. Molina Villarino, M. A. Lowe, S.-H. Yu, H. D. Abruña, *Curr. Opin. Electrochem.* **2021**, *25*, 100652.
[13] H. J. Peng, J. Q. Huang, X. B. Cheng, Q. Zhang, *Adv. Energy Mater.* **2017**, *7*, 1700260.
[14] S. Dörfler, H. Althues, P. Härtel, T. Abendroth, B. Schumm, S. Kaskel, *Joule* **2020**, *4*, 539.
[15] X. B. Cheng, C. Yan, J. Q. Huang, P. Li, L. Zhu, L. Zhao, Y. Zhang, W. Zhu, S. T. Yang, Q. Zhang, *Energy Storage Mater.* **2017**, *6*, 18.
[16] H.-S. Kang, E. Park, J.-Y. Hwang, H. Kim, D. Aurbach, A. Rosenman, Y.-K. Sun, *Adv. Mater. Technol.* **2016**, *1*, 1600052.
[17] W. Zhang, S. Li, A. Zhou, H. Song, Z. Cui, L. Du, *Molecules* **2021**, *26*, 6341.
[18] R. Song, R. Fang, L. Wen, Y. Shi, S. Wang, F. Li, *J. Power Sources* **2016**, *301*, 179.
[19] M. Weinberger, M. Wohlfahrt-Mehrens, *Electrochim. Acta* **2016**, *191*, 124.
[20] J. Guo, J. Li, H. Liu, S. Li, F. Qin, B. Hong, *Ionics* **2021**, *27*, 3347.
[21] L. Shi, S.-M. Bak, Z. Shadike, C. Wang, C. Niu, P. Northrup, H. Lee, A. Y. Baranovskiy, C. S. Anderson, J. Qin, S. Feng, X. Ren, D. Liu, X.-Q. Yang, F. Gao, D. Lu, J. Xiao, J. Liu, *Energy Environ. Sci.* **2020**, *13*, 3620.
[22] F. S. Reuter, C. J. Huang, Y. C. Hsieh, S. Dörfler, G. Brunklaus, H. Althues, M. Winter, S. D. Lin, B. J. Hwang, S. Kaskel, *Batteries Supercaps* **2021**, *4*, 347.
[23] N. Azimi, W. Weng, C. Takoudis, Z. Zhang, *Electrochem. Commun.* **2013**, *37*, 96.
[24] C. Weller, S. Thieme, P. Härtel, H. Althues, S. Kaskel, *J. Electrochem. Soc.* **2017**, *164*, A3766.

[25] C. Weller, J. Pampel, S. Dörfler, H. Althues, S. Kaskel, *Energy Technol.* **2019**, *7*, 1900625.
[26] X. Wang, Y. Tan, G. Shen, S. Zhang, *J. Energy Chem.* **2020**, *41*, 149.
[27] H. Moon, T. Mandai, R. Tatara, K. Ueno, A. Yamazaki, K. Yoshida, S. Seki, K. Dokko, M. Watanabe, *J. Phys. Chem. C* **2015**, *119*, 3957.
[28] H. Schneider, T. Weiß, C. Scordilis-Kelley, J. Maeyer, K. Leitner, H.-J. Peng, R. Schmidt, J. Tomforde, *Electrochim. Acta* **2017**, *243*, 26.
[29] T. Boenke, P. Härtel, S. Dörfler, T. Abendroth, F. Schwotzer, H. Althues, S. Kaskel, *Batterries Supercaps* **2021**, *4*, 989.
[30] D. Liu, Z. Shadike, R. Lin, K. Qian, H. Li, K. Li, S. Wang, Q. Yu, M. Liu, S. Ganapathy, X. Qin, Q. H. Yang, M. Wagemaker, F. Kang, X. Q. Yang, B. Li, *Adv. Mater.* **2019**, *31*, 1806620.
[31] J. Tan, D. Liu, X. Xu, L. Mai, *Nanoscale* **2017**, *9*, 19001.
[32] Y. Yan, C. Cheng, L. Zhang, Y. Li, J. Lu, *Adv. Energy Mater.* **2019**, *9*, 1900148.
[33] C. Zech, P. Hönicke, Y. Kayser, S. Risse, O. Grätz, M. Stamm, B. Beckhoff, *J. Mater. Chem. A* **2021**, *9*, 10231.
[34] E. Hark, S. Risse, B. Kent, R. Müller, M. Ballauff, Y. Lu, *ECS Meeting Abstracts*, ECS, **2020**, Vol. *MA2020-02*, p. 1103.
[35] S. Risse, E. Härk, B. Kent, M. Ballauff, *ACS Nano* **2019**, *13*, 10233.
[36] Y. Yang, S. Risse, S. Mei, C. J. Jafta, Y. Lu, C. Stöcklein, N. Kardjilov, I. Manke, J. Gong, Z. Kochovski, M. Ballauff, *Energy Storage Mater.* **2017**, *9*, 96.
[37] A. Ronneburg, M. Osenberg, K. Dong, A. Hilger, E. Härk, L. Silvi, I. Manke, M. Ballauff, S. Risse, *Energy Storage Mater.* **2020**, *32*, 377.
[38] L. Kong, Q. Jin, J. Q. Huang, L. D. Zhao, P. Li, B. Q. Li, H. J. Peng, X. Zhang, Q. Zhang, *Energy Technol.* **2019**, *7*, 1900111.
[39] Y. Cui, A. Abouimrane, J. Lu, T. Bolin, Y. Ren, W. Weng, C. Sun, V. A. Maroni, S. M. Heald, K. Amine, *J. Am. Chem. Soc.* **2013**, *135*, 8047.
[40] Q. He, A. T. S. Freiberg, M. U. M. Patel, S. Qian, H. A. Gasteiger, *J. Electrochem. Soc.* **2020**, *167*, 080508.
[41] M. U. M. Patel, R. Demir-Cakan, M. Morcrette, J.-M. Tarascon, M. Gaberscek, R. Dominko, *ChemSusChem* **2013**, *6*, 1177.
[42] J. Kulisch, H. Sommer, T. Brezesinski, J. Janek, *Phys. Chem. Chem. Phys.* **2014**, *16*, 18765.
[43] M. Kavčič, M. Petric, A. Rajh, K. Isaković, A. Vizintin, S. D. Talian, R. Dominko, *ACS Appl. Energy Mater.* **2021**, *4*, 2357.
[44] C. Barchasz, L. Boutafa, E. Mayousse, B. Chavillon, *Electrochim. Acta* **2018**, *292*, 974.
[45] N. Ding, X. Li, S. W. Chien, Z. Liu, Y. Zong, *Chem. Commun.* **2017**, *53*, 10152.
[46] C. Park, A. Ronneburg, S. Risse, M. Ballauff, M. Kanduč, J. Dzubiella, *J. Phys. Chem. C* **2019**, *123*, 10167.
[47] S. Risse, N. A. Cañas, N. Wagner, E. Härk, M. Ballauff, K. A. Friedrich, *J. Power Sources* **2016**, *323*, 107.
[48] A. Fotouhi, D. J. Auger, K. Propp, S. Longo, R. Purkayastha, L. O'Neill, S. Walus, *IEEE Trans. Veh. Technol.* **2017**, *66*, 7711.
[49] A. Fotouhi, D. J. Auger, L. O'Neill, T. Cleaver, S. Walus, *Energies* **2017**, *10*, 1937.
[50] M. Marinescu, L. O'Neill, T. Zhang, S. Walus, T. E. Wilson, G. J. Offer, *J. Electrochem. Soc.* **2017**, *165*, A6107.
[51] M. Wild, G. J. Offer, *Lithium-Sulfur Batteries*, John Wiley & Sons, Ltd, Chichester, UK, **2019**.
[52] C.-F. Chen, A. Mistry, P. P. Mukherjee, *J. Phys. Chem. C* **2017**, *121*, 21206.
[53] F. Y. Fan, W. C. Carter, Y. M. Chiang, *Adv. Mater.* **2015**, *27*, 5203.
[54] N. A. Cañas, S. Wolf, N. Wagner, K. A. Friedrich, *J. Power Sources* **2013**, *226*, 313.
[55] A. Schneider, C. Weidmann, C. Suchomski, H. Sommer, J. Janek, T. Brezesinski, *Chem. Mater.* **2015**, *27*, 1674.
[56] T. Danner, A. Latz, *Electrochim. Acta* **2019**, *322*, 134719.
[57] M. I. Nandasiri, L. E. Camacho-Forero, A. M. Schwarz, V. Shutthanandan, S. Thevuthasan, P. B. Balbuena, K. T. Mueller, V. Murugesan, *Chem. Mater.* **2017**, *29*, 4728.
[58] K. Yuan, L. Yuan, J. Xiang, Y. Liao, J. Chen, Y. Huang, *ACS Appl. Mater. Interfaces* **2022**, *14*, 698.
[59] Z. Liu, P. P. Mukherjee, *ACS Appl. Mater. Interfaces* **2017**, *9*, 5263.
[60] L. C. Gerber, P. D. Frischmann, F. Y. Fan, S. E. Doris, X. Qu, A. M. Scheuermann, K. Persson, Y. M. Chiang, B. A. Helms, *Nano Lett.* **2016**, *16*, 549.
[61] A. N. Mistry, P. P. Mukherjee, *J. Phys. Chem. C* **2018**, *122*, 18329.
[62] Y. Wang, E. Sahadeo, G. Rubloff, C.-F. Lin, S. B. Lee, *J. Mater. Sci.* **2018**, *54*, 3671.
[63] J. Bell, R. Ye, D. Patino, K. Ahmed, A. Scott, L. Peng, Z. Mutlu, M. Ozkan, C. S. Ozkan, *Nano Energy* **2018**, *49*, 498.
[64] Y. Han, X. Duan, Y. Li, L. Huang, D. Zhu, Y. Chen, *Ionics* **2015**, *22*, 151.
[65] X.-B. Cheng, C. Yan, X. Chen, C. Guan, J.-Q. Huang, H.-J. Peng, R. Zhang, S.-T. Yang, Q. Zhang, *Chem* **2017**, *2*, 258.
[66] S. Risse, C. J. Jafta, Y. Yang, N. Kardjilov, A. Hilger, I. Manke, M. Ballauff, *Phys. Chem. Chem. Phys.* **2016**, *18*, 10630.
[67] N. Kardjilov, A. Hilger, I. Manke, *J. Large-Scale Res. Facil. JLSRF* **2016**, *2*, A98.
[68] J. Schindelin, I. Arganda-Carreras, E. Frise, V. Kaynig, M. Longair, T. Pietzsch, S. Preibisch, C. Rueden, S. Saalfeld, B. Schmid, J. Y. Tinevez, D. J. White, V. Hartenstein, K. Eliceiri, P. Tomancak, A. Cardona, *Nat. Methods* **2012**, *9*, 676.